Corrosion Science 184 (2021) 109356

Contents lists available at ScienceDirect

Corrosion Science

journal homepage: www.elsevier.com/locate/corsci

Analysis of naturally-generated corrosion products due to chlorides in 20-year old reinforced concrete: An elastic modulus-mineralogy characterization

Emanuele Rossi [a,*], Hongzhi Zhang [b], Santiago J. Garcia [c], Johan Bijleveld [c], Timo G. Nijland [d], Oğuzhan Çopuroğlu [a], Rob B. Polder [a,d,e], Branko Šavija [a]

[a] Department of Materials & Environment, Faculty of Civil Engineering & Geosciences, Delft University of Technology, Stevinweg 1, 2628 CN, Delft, the Netherlands
[b] School of Qilu Transportation, Shandong University, 25002, Jinan, PR China
[c] Novel Aerospace Materials Group, Faculty of Aerospace Engineering, Delft University of Technology, Kluyverweg 1, 2629 HS, Delft, the Netherlands
[d] TNO Buildings, Infrastructures and Maritime, PO Box 155, 2600 AD, Delft, the Netherlands
[e] RPCP, Fluwelensingel 106, 2806 CH, Gouda, the Netherlands

ARTICLE INFO

Keywords:
Corrosion (C)
Steel reinforced concrete (A)
Raman spectroscopy (B)
XRD (B)
SEM (B)

ABSTRACT

The elastic modulus of corrosion product (E_{cp}) has been reported with significant variations in the literature. This study aims to investigate the E_{cp} of naturally-generated chloride-induced corrosion products formed in different concrete mixes. Microstructural characterization was conducted through nano-indentation, electron microscopy and Raman spectroscopy. The corrosion products were mainly composed of a goethite matrix with portions of maghemite, independently of the concrete composition. Microscopic analysis suggest that layers of corrosion products grow at different times and under different physico-chemical conditions. Our measurements showed that E_{cp} varied between 80−100 GPa, which can be suggested for numerical models of corrosion induced cracking.

1. Introduction

Chloride-induced corrosion is a major degradation mechanism affecting reinforced concrete structures. It involves dissolution of iron caused by the external chloride ion ingress through the cementitious matrix and eventually reaching the steel surface. In presence of oxygen and an electrolyte, formation of corrosion products (i.e. iron oxides and hydroxides) occurs, which exerts tensile stresses within the cementitious matrix and leads to cracking of concrete. Cracks further facilitate chloride ions to penetrate into the structure more easily and accelerate the steel corrosion [1]. In practice, excessive corrosion often results in unforeseen maintenance, repair costs and, in severe cases, loss of structural capacity. Therefore, predicting degradation of concrete due to corrosion is a vital exercise. Numerous modelling attempts have been presented in the last decade which mainly considered the degradation through assessing mechanical properties [2–6]. In these models, the elastic modulus of the corrosion (E_{cp}) products plays an important role in predicting the crack development over time within the concrete cover [7], since corrosion products forming at the steel/concrete interface (SCI) participate in the mechanical interaction between the rebar and cementitious matrix when corrosion occurs. Depending on the model, the used E_{cp} can have significant impact on the accuracy of the predicted time to cracking [8]. Hence, one of the major challenges to make better predictive models is to obtain accurate values of E_{cp}.

Many studies have been attempted to determine a realistic value of E_{cp} that can be used in concrete fracture models [7–19]. Samsonov [9] assumed that the elastic modulus of iron oxides ranged between 215 GPa and 350 GPa. Similar values were estimated by Ouglova et al. [10], who obtained a value of E_{cp} of 360 GPa through oedometer test on rust samples. Bhargava et al. [11] assumed that E_{cp} was the same as that of low-carbon steel (i.e. 207 GPa). It seems, however, unlikely that E_{cp} would be comparable (or even be higher) than the elastic modulus of a pristine steel due to the differences in hardness and microstructural density values of the both phases [12]. Also, corrosion products may contain different concentration of oxygen and hydrogen, which influence the inter-atomic bonding energy and, hence, the modulus of elasticity of the compound. Lower E_{cp} values were measured by Housemann et al. [13], who performed nano-indentation on corrosion products and

* Corresponding author.
E-mail address: e.rossi@tudelft.nl (E. Rossi).

https://doi.org/10.1016/j.corsci.2021.109356
Received 19 October 2020; Received in revised form 24 February 2021; Accepted 26 February 2021
Available online 2 March 2021

observed that E_{cp} ranged between 70−100 GPa. The same authors also found two distinct layers (inner and outer) of corrosion products when inspecting samples with Scanning Electron Microscopy (SEM). A similar distinction was observed also by Zhao et al. [7]. In this case, nano-indentation unveiled that the E_{cp} of the inner layer ranged between 47−86 GPa while the E_{cp} of the outer layer ranged between 98−122 GPa. The same technique was used by Šavija et al. [8], who measured the E_{cp} of anodically-accelerated corrosion products. In their study, no distinction between rust layers was observed through SEM analysis, and their E_{cp} values ranged between 50−68 GPa. A thorough research was conducted by Derhoux et al. [14], who coupled nano-indentation, Raman spectroscopy and Scanning Electron Microscope (SEM) analysis to characterize corrosion products at the SCI of differently corroding samples. In their study, they obtained characteristic values for specific corrosion product phases, which were 92−95 GPa for goethite, 56 GPa for ferrihydrate, 113 GPa for maghemite/ferrihydrate and 139 GPa for magnetite/maghemite. Similarly, Jiang et al. [15] coupled nano-indentation and Raman spectroscopy to characterize corrosion products formed due to anodic polarization of the steel reinforcement. Differently from Dehoux et al. [14], they found 67.9 ± 5.3 GPa for goethite/lepidocrocite, 69.4 ± 2.9 GPa for akaganeite, 82.3 ± 3.7 GPa for maghemite and 103.2 ± 2.7 GPa for magnetite. For both studies, these values were consistent for similar phases found in different specimens within the same study. Lundgren [16] proposed a stress-strain formula to determine the mechanical properties of corrosion product, based on the two-dimensional relation between the three components at the SCI (steel, corrosion product and concrete), which resulted in E_{cp} of 14 GPa. Suda et al. [17] found that E_{cp} ranged between 0.1−0.5 GPa through nonlinear finite element analysis. Carè et al. [18] devised two hollow cylinder models using the elastic mechanics method, through which they determined E_{cp}. For their first model, the Elastic modulus of the rust layer was deduced as equal to 140 MPa, while for their second model, E_{cp} ranged between around 50 MPa and 250 MPa. Interestingly, they concluded that E_{cp} was dependent on the thickness of the rust layer and on the initial radius of the reinforcement, and that a constant value for E_{cp} should not be considered in numerical modelling [18]. Balafas [19] proposed E_{cp} of 40−87 MPa, while Zhao [12] proposed 100 MPa after performing cyclic low-compression and oedemeter tests on naturally-generated corrosion products. In their model for concrete cover cracking as a function of steel corrosion, Molina et al. [20] tested values of E_{cp} of 2.0–4.0 GPa, with no relevant influence on the output results. Studying the elastic modulus of corrosion product, Molina et al. [20] assumed that corrosion product was perfectly elastic and that it could be considered as a fluid with Poisson's ratio (v_r) of 0.5 and bulk modulus (K_r) of 2.0 GPa. Using the equation $E_{cp} = 3(1-2v_r)*K_r$, they run their models with E_{cp} of 12 MPa.

Fig. 1 shows the significant variations related to E_{cp} according to the existing literature. Such broad variations might be attributed to the different methods used to characterize corrosion products and their micro-mechanical properties as well as to the different types of corroding conditions (i.e. atmospheric, anodically-accelerated, chloride-induced, etc.) to which specimens were subjected.

1.1. Aim of the study

A survey on the existing literature revealed that the effect of concrete mix design on the mechanical properties of corrosion products is not sufficiently understood. Therefore this study aimed to look into a possible relationship between the type of cement and the mechanical properties and mineralogy of naturally-generated chloride-induced corrosion products. E_{cp} was obtained through nano-indentation of corrosion product formed at the SCI. A comparison between the results of this study and E_{cp} proposed by others was made, especially regarding the elastic moduli obtained with the same technique [7,8,13–15]. Raman Spectroscopy, ESEM (Environmental Scanning Electron Microscope) observations and EDS (Energy Dispersive Spectrometry) elemental mapping were included in this study to investigate the relation between the mechanical properties and elemental composition and mineralogy of corrosion products. The different mineralogy of the corrosion products was analysed with regard to the cementitious matrix in which they were embedded. Characterization of corrosion products present at the SCI would help to better understand which compounds were formed under certain conditions and how (trans)formation of corrosion products would occur during time. These information aim to better understand the development of steel corrosion in concrete.

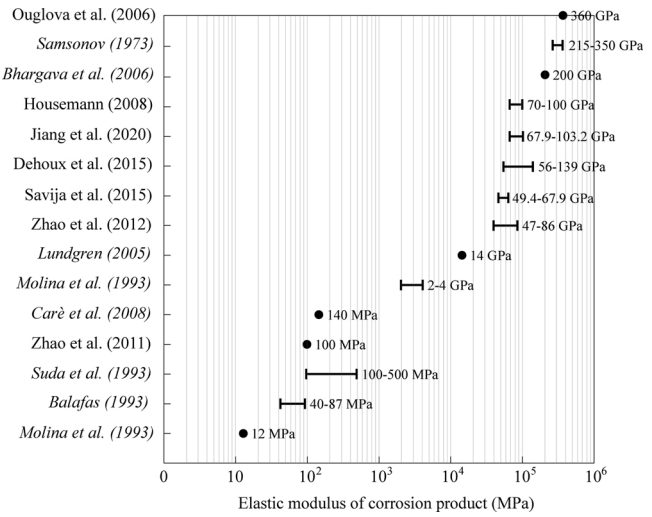

Fig. 1. Elastic moduli of corrosion products (E_{cp}) according to the literature (experimentally measured E_{cp} values appear in regular font and estimated and/or modelled E_{cp} values in italic).

2. Materials and methods

2.1. Specimen preparation

In this work, polished sections of four reinforced concrete were analysed through nano-indentation, Raman spectroscopy, microscopic analysis and EDS elemental mapping. The polished sections were obtained from 20-year-old prisms cast in 1998 by Polder & Russo [21]. The prisms were cast with four different cement types (CEM I, CEM II/B–V, CEM III/B, CEM V/A), with a water/binder ratio (w/b) of 0.55 and using siliceous river material with a maximum diameter (D_{max}) of 8 mm as aggregate. In each prism, two groups of three smooth carbon steel bars (S235) of 8 mm in diameter were embedded at a depth of 10 mm and 30 mm away from the mould face (Fig. 2). Prior to casting, each bar was prepared by light polishing with sandpaper and cleaned in acetone. A coat of cement paste and subsequently a coat of dense epoxy coating were applied to both ends of the bar to minimize any side effect, leaving an exposed length of 45 mm starting at 10 mm from the top side of the prism. Two activated titanium wire electrodes (Ti*) and four stainless steel bars were also part of the specimens' layout, but they were not considered in this study. After casting, prisms were exposed to 3.5 % NaCl solution wet/dry cycles (1 day wet/6 days dry) for 6 months and later left directly exposed (unsheltered) to the outside environment in Delft, the Netherlands. The concrete compositions are summarized in Table 1.

For this study, one cylindrical core of 20 mm in diameter was drilled out from each prism. Each core contained a single rebar along its axis, as described elsewhere [22]. The steel bar had 10 mm of cover depth. The cores were vacuum impregnated by low viscosity fluorescent epoxy. After the epoxy was cured, the cores were carefully sawn perpendicularly to the bars, obtaining one 5-mm-high slice per each core. Once sawn, sections were manually ground with #120, #220, #320, #600, #800 and 1200# silicon carbide sanding paper and polished with 6, 3, 1

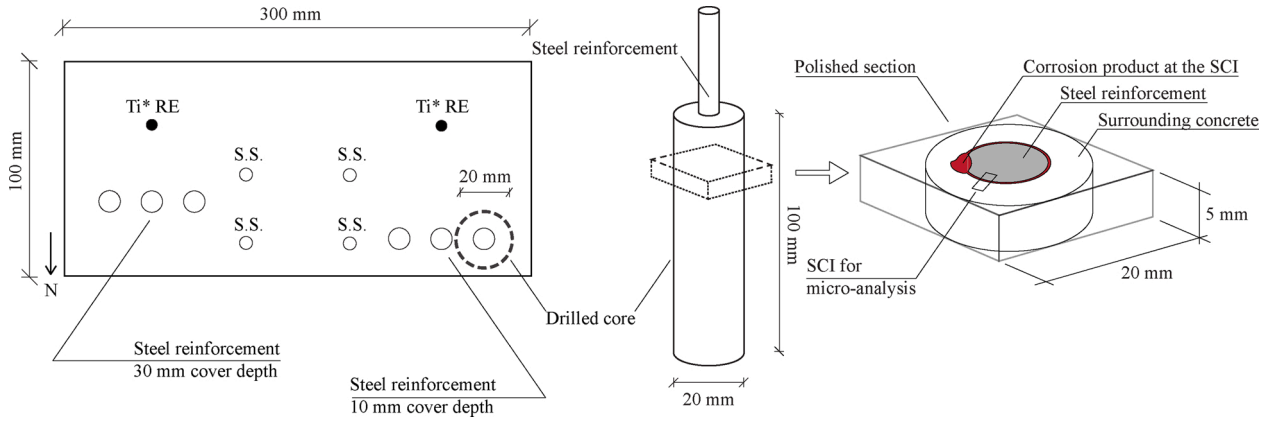

Fig. 2. (left) top view of the prismatic specimen; (centre) drilled reinforced concrete core; (right) reinforced concrete section subjected to micro-analysis after impregnation, sawing, grinding and polishing (S.S. = stainless steel; Ti*Re = activated Titanium electrode; N = direction towards the outdoor environment).

Table 1
Mix proportions for each specimen (w/b of 0.55; D_{max} of 8 mm) [21].

Specimen	Cement type	Portland cement content (kg/m^3)	Fly ash content (kg/m^3)	Slag content* (kg/ m^3)	Aggregate content (kg/ m^3)
S1	CEM I 32.5 R Portland cement	287	0	0	1827
S2	CEM II/B–V 32.5 R (27% fly ash)	204	76	0	1830
S3	CEM III/B LH HS 42.5 (75 % slag)	71	0	215	1864
S4	CEM V/A 42.5 (25 % fly ash, 25 % slag)	139	70	70	1839

* ground granulated blast furnace slag.

and 0.25 μm polishing diamond paste on a lapping table to obtain a mirror-like surface of the specimens. Each grinding and polishing step took around 10 min. Ethanol and non-water based polishing paste were used for grinding and polishing, respectively, to avoid further on-going corrosion. Once polished, sections were coated with commercial transparent nail polish to protect the polished section from oxygen. Just prior to conducting the experiments, nail polish was removed by acetone and the surfaces were reconditioned with 0.25 μm diamond paste for around 15 min. A representation of the whole sample preparation procedure is reported in Fig. 2.

2.2. Experimental techniques

2.2.1. Nano-indentation

Nano-indentation was conducted on the corrosion product formed at the SCI. Suitable locations to conduct the experiment (i.e. significant amount of corrosion product) were located by optical stereomicroscope (Leica MZ6). A KLA-Tencor Nano Indenter G200 with diamond Berkovich tip (i.e. a three-side pyramidal diamond) was used for the experiment, as conducted by Šavija et al. [8]. Each polished section was subjected to one grid-like series of 100 indents, with fixed row/column number (i.e. 5/20) and spacing between each indent (20 μm). E_{cp} was determined through the Continuous Stiffness Method (CSM) developed by Oliver and Pharr [23], which continuously measures the stiffness of the indented material as a function of indentation depth. The maximum indentation depth was set at 2000 nm. The output E_{cp} was the average of the values measured between 1000 nm and 1800 nm. The Poisson's ratio of corrosion product was set at 0.25 similar to what was used in other studies on nano-indentation of corrosion products [7,8]. Prior to each test, calibration of the nano-indenter was conducted on external quartz standards. An example of two measurements of elastic modulus (one for steel and one for corrosion product) is visible in Fig. 3.

In Fig. 3 it is visible that in the shallow indentation depth, the elastic modulus measurements fluctuate up to very high values (i.e. 350 GPa for steel) because of the roughness of the sample surface [7]. However, as the indentation depth increases, the elastic modulus lines converge to overall constant values deeper than 1000 nm, especially for corrosion products. Therefore, the values that are measured at the depth range of 1000−1800 nm are representative for the average elastic modulus of each indent. It is worth mentioning that some portions of indented corrosion products and surrounding matrix were significantly cracked, as visible later in this manuscript. As a consequence, the resulting elastic modulus for certain indents was equal to 0 GPa. These values have been included in the elastic modulus maps of Figs. 9–12, but they have not been considered for further analysis (i.e. the average elastic modulus of corrosion products for each sample visible in Fig. 18).

2.2.2. Scanning electron microscopy (SEM) with energy dispersive spectroscopy (EDS)

SEM and NanoSEM observations were conducted to identify the locations where nano-indentation was performed as well as to study the textures morphology of corrosion products. The SEM used was a Philips XL30 ESEM. For the microanalysis, it was operated at 20 kV accelerating voltage and standard-based microanalysis protocols were used from

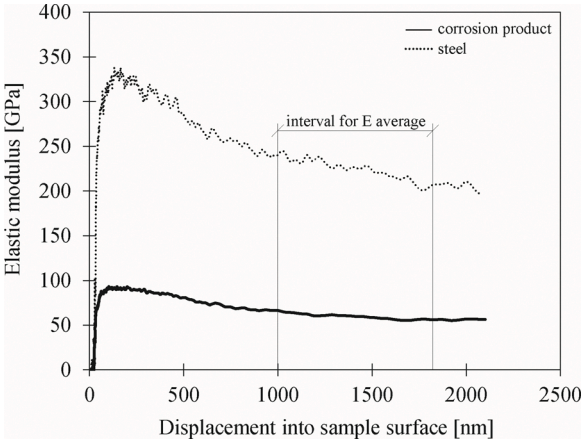

Fig. 3. Example of elastic modulus measurements for steel and corrosion product.

[24]. Backscattered electron (BSE) images were acquired with a magnification of x200. To investigate the relation between the chemical composition and the elastic modulus of corrosion products, EDS elemental maps were also acquired at 20 kV. In addition, textures were studied using a FEI Nova NanoSEM 650 at TNO, using a solid state GAD detector, operated at 10 kV.

2.2.3. Raman spectroscopy

The portions of corrosion product subjected to nano-indentation and ESEM/EDS analysis were further characterized by Raman spectroscopy spot analysis. Raman spectroscopy tests were performed using a Raman InVia reflex microscope (Renishaw) with an acquisition time of 1 min. The spectral region from 300 to 1500 cm^{-1} was collected using a laser with an excitation line of 785 nm. The peak area was calculated using a peak analyser tool from Origin, the baseline was subtracted, and the peak was fitted to a Gaussian fit. The different corrosion product phases were identified by comparing the obtained spectra with reference spectra from the current literature [14,15,25–27].

2.2.4. X-ray diffraction (XRD)

X-ray diffraction analysis (XRD) was performed on powdered samples obtained from the liberated rebars. XRD was performed using a Bruker D8 Advance diffractometer equipped with a Lynxeye detector with opening angle of 2.94°, working at 40 kV and 40 mA. The data of the experiment were collected at room temperature using Cu Kα radiation (λ =1.5406 Å) over a 2θ range of 10°-40°, step size 0.02 degrees 2θ. The sample was deposited on a zero background holder and was rotated at 15 rpm during the measurement. Generator settings were 40 kV and 40 mA. After data collection, phase identification was carried out with the Bruker program EVA4.2 and based on expert judgement.

3. Results

In the first part of this section, a textural description of the corrosion products based on SEM analysis at or near the SCI is presented. In the second part, the mechanical and compositional characterization of these corrosion products is shown. The experimental investigations and analysis reported in this study are representative of limited areas at the SCI of different specimens, which however did not significantly differ from the other locations around the reinforcement visually. Therefore, the analysed locations were considered to be representative of the entire SCI for a given specimen.

3.1. Corrosion product textures

In sample S1 (Fig. 4), two layers of corrosion products were present around the steel. These occur within a very thin (around 5 in all samples), bright (i.e. high electron back-scattering due to a relatively high average atomic number) layer considered to represent the original mill scale layer as reported by other studies [7,13]. Even though the rebars were polished before casting, it is likely that the whole mill scale layer could not be removed. As a consequence, in all the samples of this study the remaining of the original mill scale layer is thinner than 10−20 μm as reported by Cook [28]. At the interface between the internal corrosion layer and the steel, tiny dark grey indents are visible. In addition, an air void was present just outside these corrosion layers, separated from it by a thin cement paste interlayer of about 20 μm wide. The air void was filled by corrosion products.

In sample S2 (Fig. 5), the corrosion products were present in a layer around the steel. The layer was convex towards the steel, with internal cracking more or less following the outline of the rebar, the widest one present more or less coinciding with the mill scale or just within the outer part of the corrosion products layer. Within the overall grey corrosion product layer, thin, slightly lighter veinlets occupied voids exist. The veinlets show tiny cracks in their middle. No air void is present, but at the interface with surrounding concrete, cracks occur with massive corrosion products along their margins and penetrating the surrounding paste.

Sample S3 (Fig. 6) shows a texture to some extent comparable with that in sample S2. The layers were also convex towards the rebar, with the inner part showing lighter marblings. Outwards, a more homogenous zone occurs, with an lighter outermost zone against the mill skin. This zone was still convex. Outside the mill skin, an area occurs with interstitial corrosion products in the cement paste. No air void was present at the SCI, but corrosion products penetrating the surrounding paste was visible.

Sample S4 (Fig. 7) shows two homogeneous grey, slightly convex layers of corrosion products against the steel, followed by a partly lighter, more marbled layer against the mill scale. This zone shows with internal cauliflower-like textures, especially in its inner part. In this zone, a crack more or less following the outline of the steel was present, coincident to the circumference of the mill scale. An air void filled with corrosion products is present just outside the mill scale.

Fig. 8 shows details of the internal microstructure within the a layer of corrosion products formed in S4 not subjected to nano-indentation. Between the corroding steel and the mill scale layer, corrosion products occupied the volume that was originally pristine steel. At this location, corrosion products look dense and compact, embedding

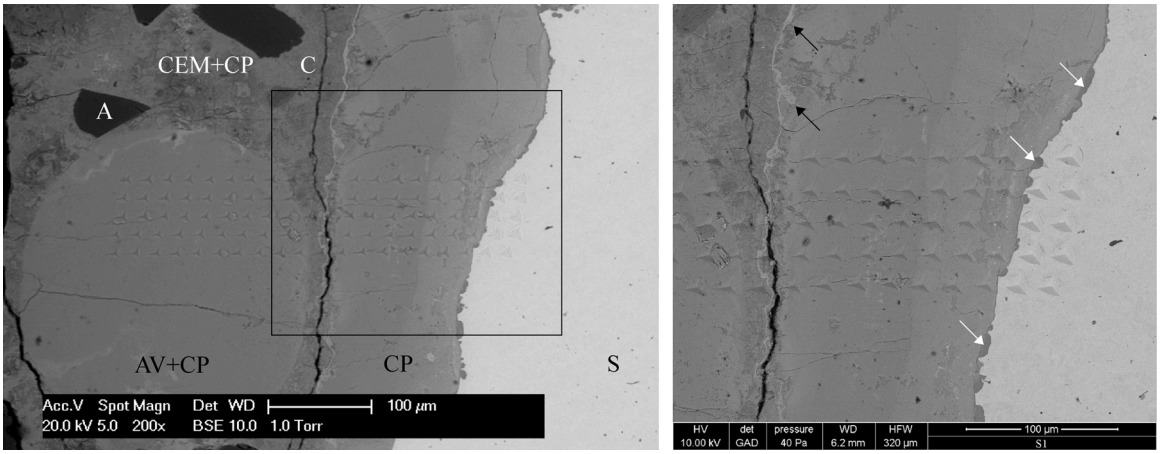

Fig. 4. S1 (left) ESEM/BSE image of indented location (S = steel; CEM = cement paste; CP = corrosion product; A = aggregate; AV = air void; C = crack). (right) SEM micro-picture (zoom-in of the box from the left figure) showing the tiny dark grey indents in the steel at the interface with the internal corrosion products layer (indicated by white arrows). The mill scale layer is indicated by black arrows.

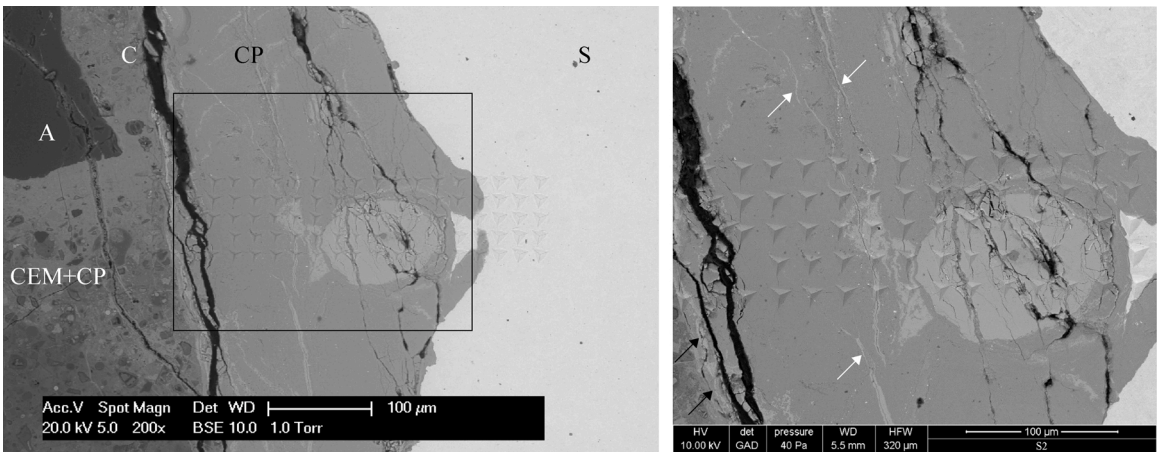

Fig. 5. S2 (left) ESEM/BSE image of indented location (S = steel; CEM = cement paste; CP = corrosion product; A = aggregate; C = crack). (right) SEM micro-picture (zoom-in of the box from the left figure) showing the tiny lighter veinlets (indicated by white arrows) and the filled hole of the same grey intensity right to the centre of the picture. The mill scale layer is indicated by black arrows.

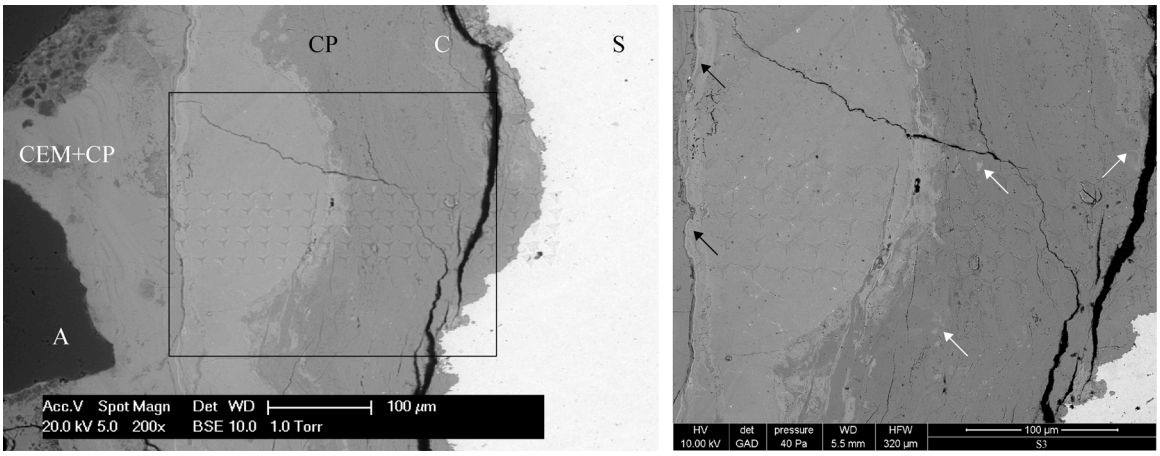

Fig. 6. S3 (left) ESEM/BSE image of indented location (S = steel; CEM = cement paste; CP = corrosion product; A = aggregate; C = crack). (right) SEM micro-picture (zoom-in of the box from the left figure) showing the lighter marblings (indicated by white arrows) and longitudinal cracks in the inner corrosion product layer. The mill scale layer is indicated by black arrows.

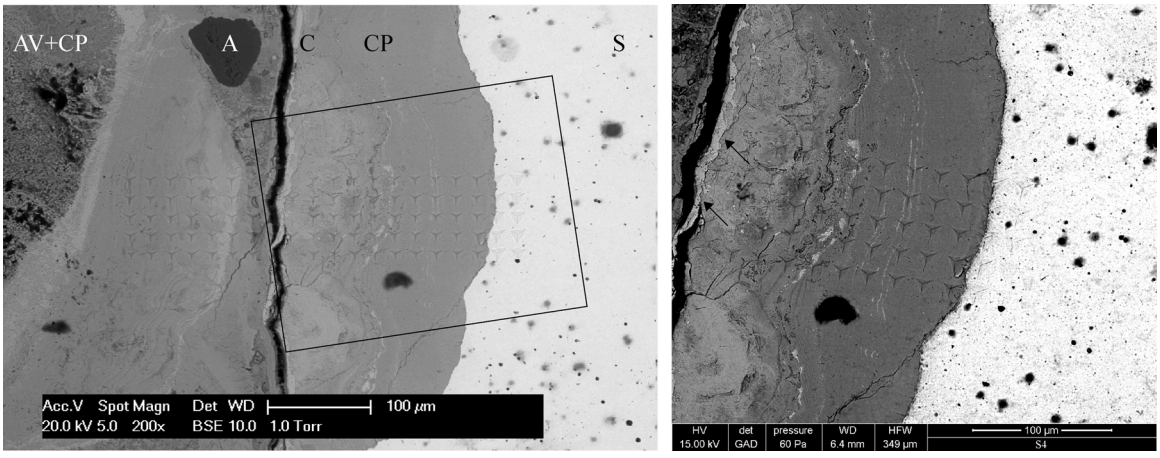

Fig. 7. S4 (left) ESEM/BSE image of indented location (S = steel; CP = corrosion product; A = aggregate; C = crack; AV = air void). (right) SEM micro-picture showing (zoom-in of the box from the left figure) the crack surrounding the steel reinforcement coincident to the mill scale layer. The mill scale layer is indicated by black arrows.

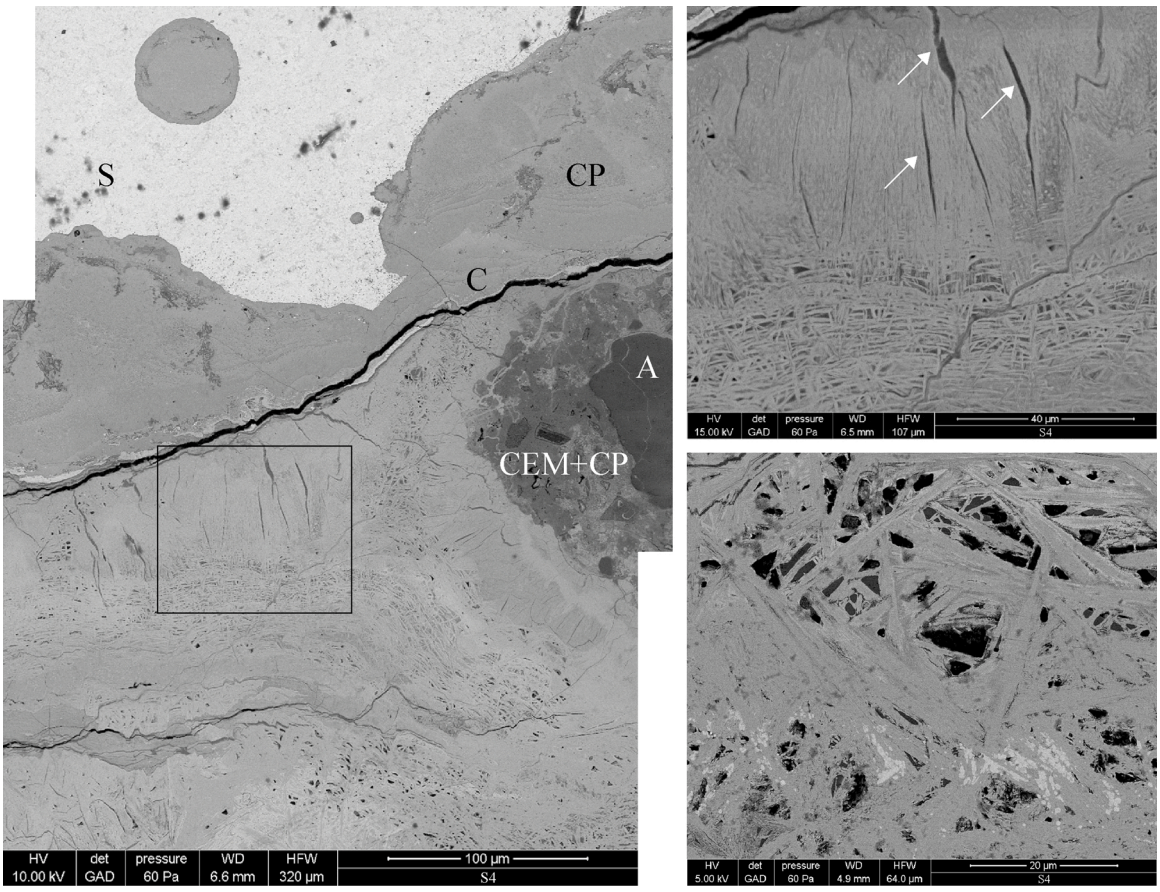

Fig. 8. S4 (left) SEM micro-image of corrosion products formed at the SCI and penetrating in the surrounding matrix with different textures and orientation (S = steel; CP = corrosion product; A = aggregate; C = crack; AV = air void). (top-right) SEM micrograph showing (zoom-in of the box from the left figure) distinct layers of corrosion products with longitudinal cracks (indicated by white arrows) and layers of variably-oriented products. (bottom-right) SEM zoom-in of corrosion products with.

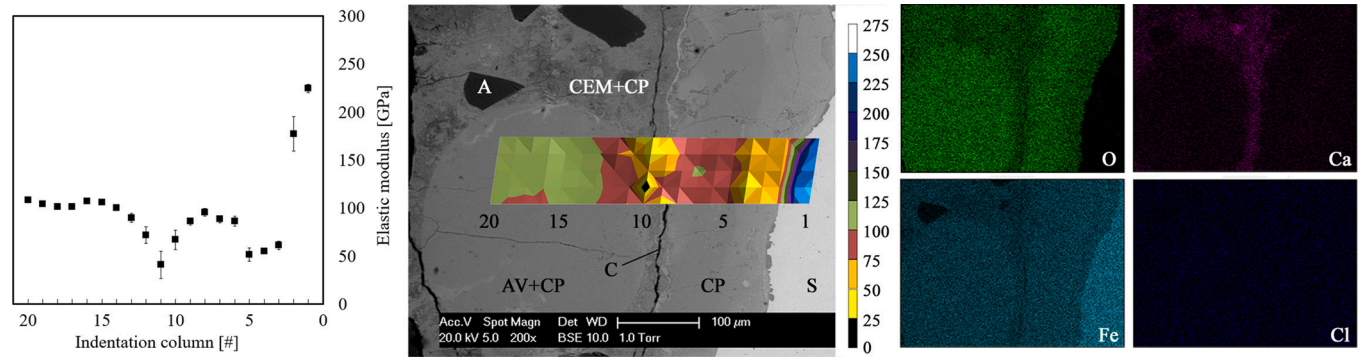

Fig. 9. S1 (left) range of E_{cp} for each column of indents; (centre) BSE image of indented location with distribution of E_{cp} (S = steel; CEM = cement paste; CP = corrosion product; A = aggregate; AV = air void; C = crack). Numbers in black indicate the columns of the indentation grid; (right) EDS elemental mapping of O, Fe, Ca, Cl.

darker-grey (i.e. lighter atomic mass) marblings in its matrix. Corrosion products also penetrated into the mill-scale layer as well as the surrounding paste. The inner part of the penetrated products was composed of discrete elongated crystals more or less perpendicular towards the original outline of the steel (Fig. 8, top-right). In these zones, cracks with the same orientation occur. The outer part is also made up by elongated crystals, but with random orientation (Fig. 8, bottom-right). These euhedral crystals enclose interstitial pores whose shape is defined by the crystal phases of the corrosion products. The textures strongly suggest different growth phases under different physio-chemical conditions.

3.2. Corrosion product characterization

In Figs. 9–12, the range of E_{cp} at the SCI for different specimens is visible, as well as the ESEM/EDS analysis and elemental mapping of the same locations. In the centre of each figure, a BSE micrograph of the indented locations at the steel/concrete interface was shown. The indented locations were overlapped by an E_{cp} map, which consist of 100 indents (divided in 5 rows and 20 columns). On the left-hand side of each figure, the E_{cp} profile is reported. Each point of the E_{cp} profile is the average of 5 indents belonging to the same indentation column. The

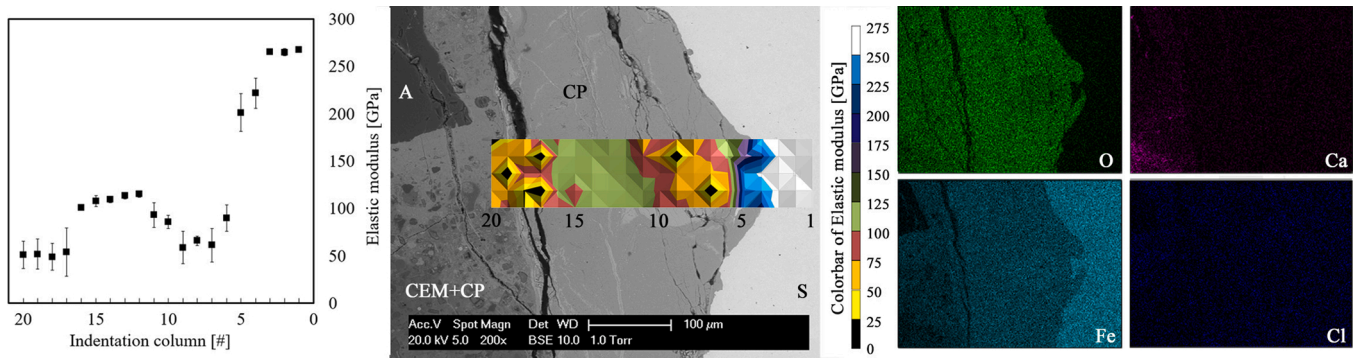

Fig. 10. S2 (left) range of E_{cp} for each column of indents; (centre) BSE image of indented location with distribution of E_{cp} (S = steel; CEM = cement paste; CP = corrosion product; A = aggregate; AV = air void; C = crack). Numbers in black indicate the columns of the indentation grid; (right) EDS elemental mapping of O, Fe, Ca, Cl.

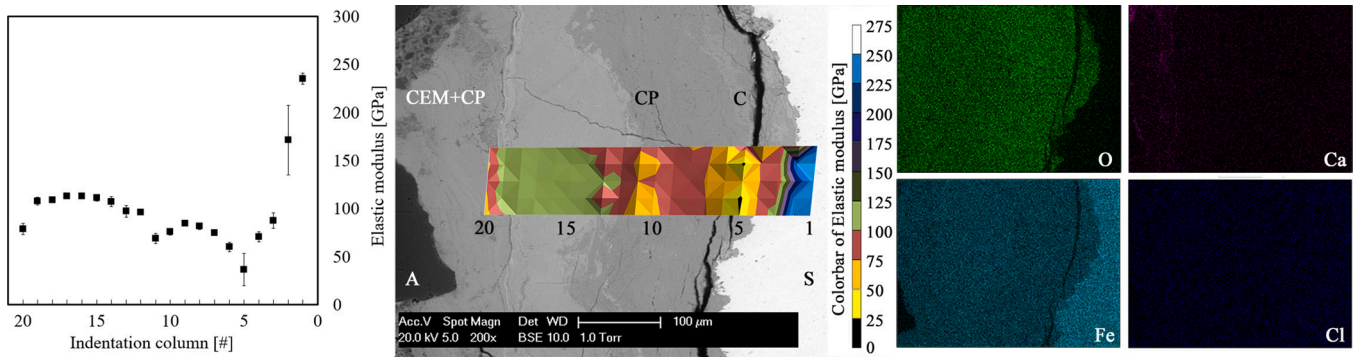

Fig. 11. S3 (left) range of E_{cp} for each column of indents; (centre) BSE image of indented location with distribution of E_{cp} (S = steel; CEM = cement paste; CP = corrosion product; A = aggregate; AV = air void; C = crack). Numbers in black indicate the columns of the indentation grid; (right) EDS elemental mapping of O, Fe, Ca, Cl.

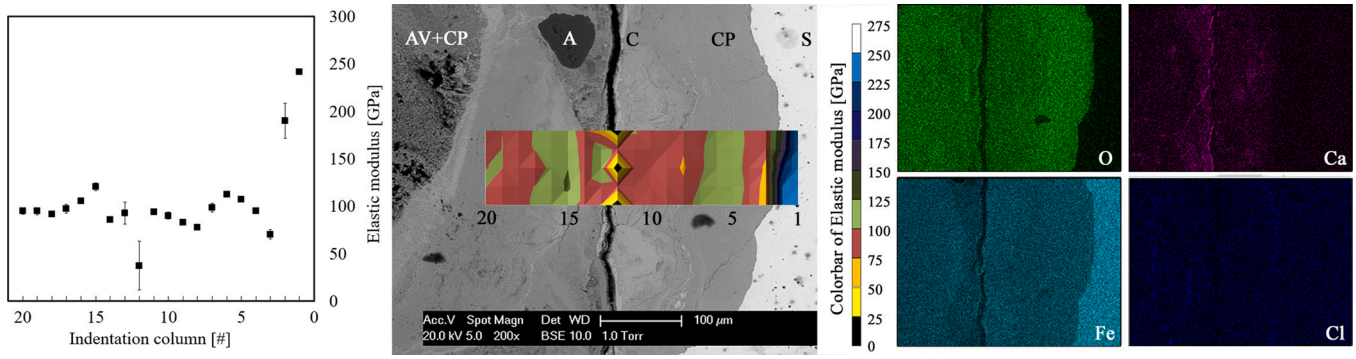

Fig. 12. S4 (left) range of E_{cp} for each column of indents; (centre) BSE image of indented location with distribution of E_{cp} (S = steel; CEM = cement paste; CP = corrosion product; A = aggregate; AV = air void; C = crack). Numbers in black indicate the columns of the indentation grid; (right) EDS elemental mapping of O, Fe, Ca, Cl. variable orientations.

variation between these values is represented by two whiskers. On the right-hand side of each image, the EDS elemental mapping of Fe, O, Ca and Cl of each indented location is reported.

Nano-indentation and SEM/EDS analysis were coupled with Raman spectroscopy of specific locations of the corrosion product at the SCI to investigate the relation between mechanical properties and mineralogy of corrosion product compounds, as reported in Figs. 13–16. In each Raman spot graph only the most representative peaks for the different corrosion products have been highlighted. When peaks of Raman spectra were not representative of any corrosion products, they were considered to be caused by signal noise and therefore remained unassigned. A schematic representation of the nano-indentation maps and the Raman spectra of each sample is given in Fig. 17.

In Figs. 9–16, areas of corrosion product with different grayscale value and E_{cp} can be distinguished, as schematically summarized in Fig. 17. As described above, sample S1 shows two layers of corrosion products around the steel (Fig. 4). The inner layer is mainly composed of goethite with minor ferrihydrate and has E_{cp} of 50−75 GPa, whereas the outer layer is also dominated by goethite, but with maghemite instead of ferrihydrate; this layer has an E_{cp} of 75−100 GPa (Figs. 9,13). The corrosion product in the interfacial air void is also goethite, with E_{cp} varying from 75 to 125 GPa. In S2 (Figs. 10,14), the matrix of the corrosion product layer is mainly composed by goethite (Fig. 14, spot 1 & 4) with an E_{cp} of 100−125 GPa. In these matrix, a zone with brighter

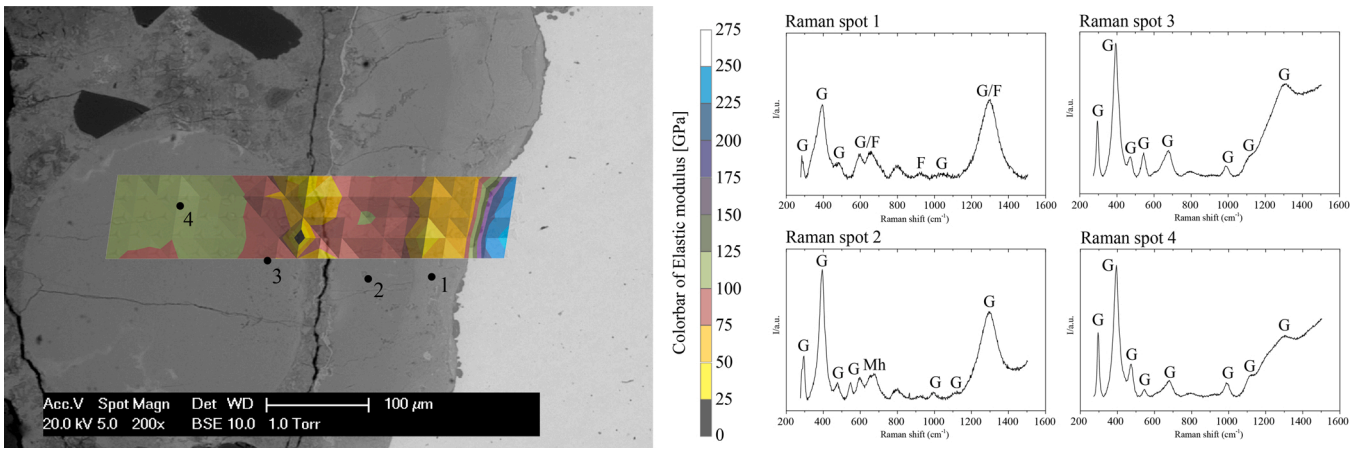

Fig. 13. S1 (left) BSE image of indented location with E_{cp} mapping (in black: spots analysed through Raman spectroscopy); (right) Raman spectra for points 1-4. (G: goethite, F: ferrihydrate; Mh: maghemite, /: coexistence of both products).

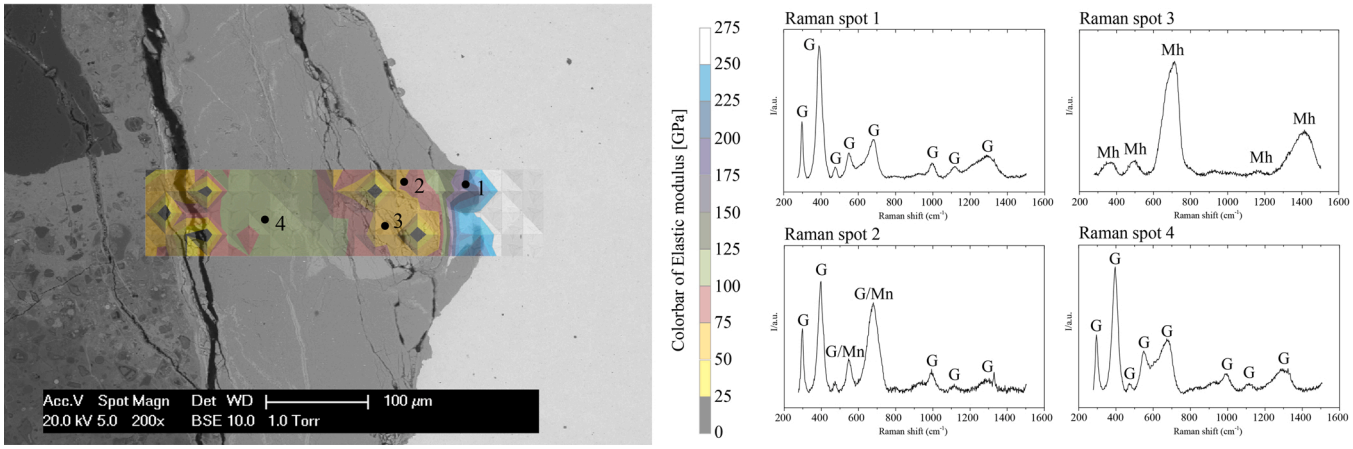

Fig. 14. S2 (left) BSE image of indented location with E_{cp} mapping (in black: spots analysed through Raman spectroscopy); (right) Raman spectra for points 1-4. (G: goethite; Mn: magnetite; Mh: maghemite, /: coexistence of both products).

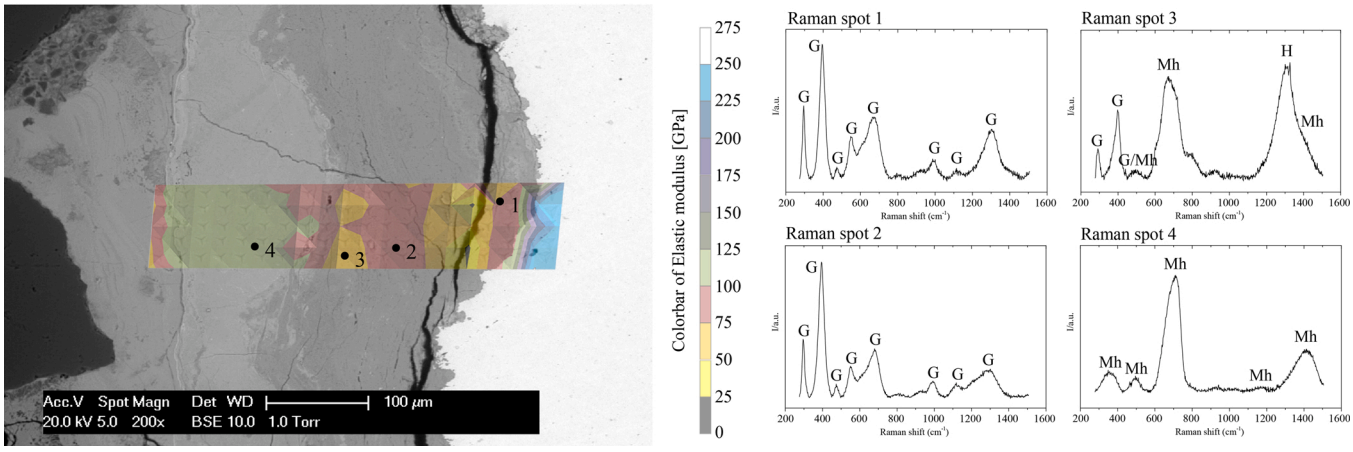

Fig. 15. S3 (left) BSE image of indented location with E_{cp} mapping (in black: spots analysed through Raman spectroscopy); (right) Raman spectra for points 1-4. (G: goethite; H: hematite; Mh: maghemite, /: coexistence of both products).

marblings and cracks as well as a filled hole are present (Fig. 5), corresponding to a mixture of goethite and magnetite (Fig. 14, spot 2) and sole maghemite (Fig. 14, spot 3), respectively. For the latter domain, a relatively low E_{cp} of 25−75 GPa was measured, at least the lower values likely due to the presence of cracks. A layered microstructure of corrosion product was also visible for S3 (Figs. 6,11). The inner layer was composed of goethite (Fig. 15, spots 1 & 2), with domains of maghemite and hematite (Fig. 15, spot 3), and E_{cp} of 50−100 GPa. The outer layer against the mill scale is made up by maghemite solely (Fig. 15, spot 4), with E_{cp} of 100−125 GPa. The two homogeneous grey

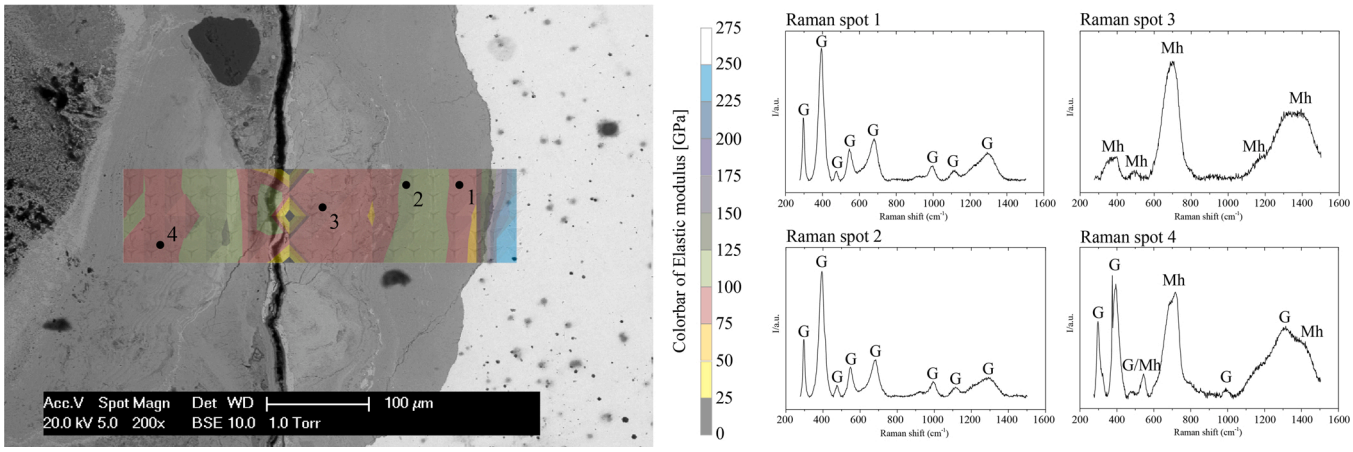

Fig. 16. S4 (left) BSE image of indented location with E_{cp} mapping (in black: spots analysed through Raman spectroscopy); (right) Raman spectra for points 1-4. (G: goethite; Mh: maghemite, /: coexistence of both products).

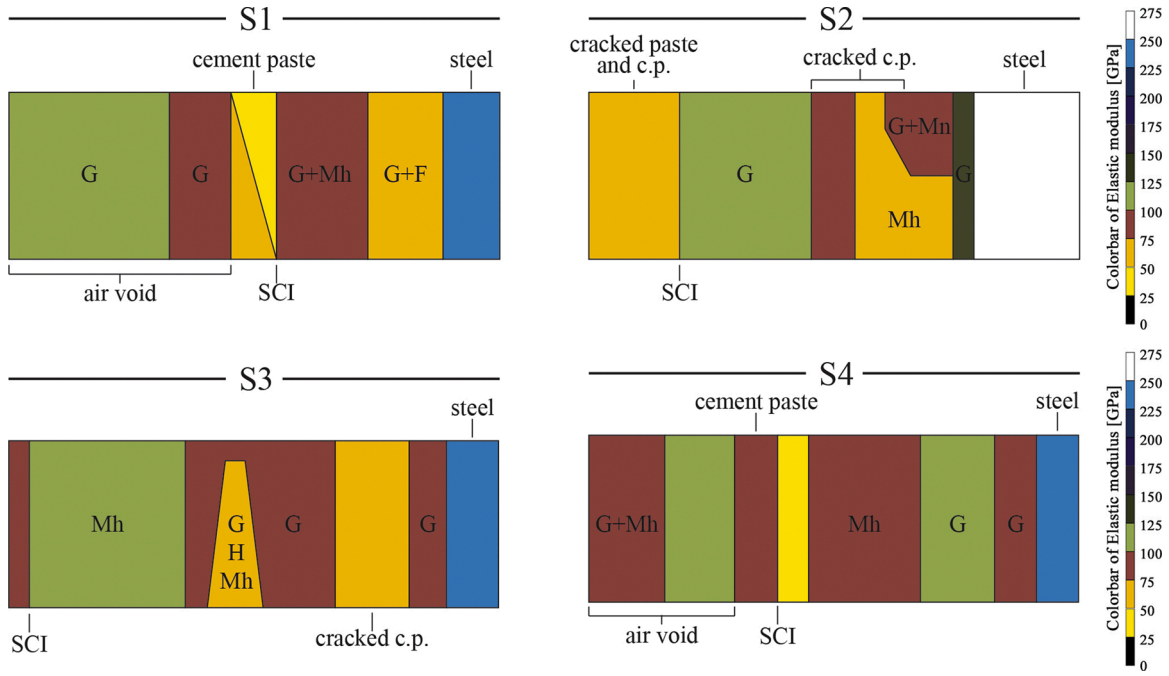

Fig. 17. Schematic representation of the nano-indentation maps and results of Raman spectroscopy for each sample. (G: goethite, F: ferrihydrate; Mh: maghemite, Mn: magnetite, H: hematite, SCI: steel/concrete interface).

layers of corrosion products in S4 (Fig. 16, spot 1 & 2) are both made up by goethite, but with an increase of E_{cp} from 75 GPa to 125 GPa close to the steel. The lighter outer layer of corrosion products adjacent to the mill scale is made up by maghemite (Fig. 16, spot 3), with E_{cp} of 75−100 GPa (Fig. 12). The corrosion products in an interfacial void partially filled are made up by a mixture of goethite and maghemite (Fig. 16, spot 4).

For all the specimens, the elastic modulus of some areas of pristine steel was higher than the known elastic modulus of low-carbon steel, equal to around 210 GPa. For S1, S3 and S4, the elastic modulus of steel was ranging between 200−250 GPa, while for S2 it reached a maximum value of about 275 GPa.

The identification of corrosion products was accompanied by powder XRD. Besides phases from the cement pastes, the following corrosion products were identified in the powders: S1 – goethite, S2 – goethite, lepidocrocite, S3 – goethite, lepidocrocite, S4 – goethite, lepidocrocite.

4. Discussion

4.1. Development of corrosion products in time

A better understanding of propagation of corrosion and its consequences does not only require determination of their mechanical properties, but also their development in time, both geometrically and mineralogically. In literature, different iron hydroxides and oxides have been reported: the four modifications of FeOOH (goethite, α-FeOOH; akaganeite, β-FeOOH; lepidocrocite, γ-FeOOH; feroxhyte, δ-FeOOH), different modifications of Fe_2O_3 (hematite, α- Fe_2O_3; maghemite, γ-Fe_2O_3), magnetite (Fe_3O_4), wüstite (FeO) and ferrihydrite ($Fe_{10}O_{14}(OH)_2$) as well as poorly crystalline or amorphous iron compounds [14,15,27,33–36]. In our samples we found goethite (and ferrihydrite in one layer in one sample) and iron oxides (mainly maghemite, also hematite and magnetite). After a period of 20 years natural chloride induced corrosion, mineralogy of corrosion products

seems to be independent with respect to the type of cement used, despite the different pH of the pore solution of different mixes. In our opinion, the different pore solution's pH does not play a role during the initial stage of corrosion products getting formed, since the very low (acid) pH at the pit depth would be more dominant than the one of the pore solution to influence the formation of the oldest (i.e. initial) compounds (goethite). On the other hand, the contact with solutions with different pH might influence how corrosion products (re)precipitated during the many-years exposure of the specimens, which however did not show any significant difference. As a consequence, the pH of the pore solution of different mixes seems a secondary factor that might influence the mineralogy of corrosion products.

The mutual relationships of the different iron compounds getting formed at the SCI, in terms of time and/or different physio-chemical conditions, has only sparsely been studied. The mineralogical interpretation of their textures is an essential prerequisite to this, though these textures might prove ambiguous. In our samples, we saw different textures:

One or two layers between the pristine steel and the mill scale (S1, S2, S3). – The fact that these occur within the mill scale and are convex towards the steel is considered as evidence that they were developed in situ (Figs. 4–6). In case of S1 and S3, the outer formation was dominated by maghemite, the inner one by goethite; in case of S2, the single layer was dominated by goethite. The presence of goethite as the dominant corrosion product around the reinforcement was in good agreement with previous studies [29–32]. Formation of goethite, as well as transformation of other FeOOH-polymorphs into goethite, could be expected since goethite is the most stable oxyhydroxide [37]. According to Song et al. [38], ferrihydrite is formed directly from the corroding mild steel and, when in contact with low Cl- content environments, transformed into goethite. Also, in a high Cl- content, lepidocrocite might evolve to goethite through chlorination, which involves the intermediate formation of β-$Fe_8O_8(OH)_8Cl_{1.35}$ [38].

Marblings and elongated streaks within the goethite layer (S1, S2, S3) – Such domains were irregularly shaped and discountinuous streaks that differ in texture and composition from the main matrix (goethite). They were composed by iron oxides (maghemite, hematite, magnetite) instead of iron hydroxides (goethite). Although it was tempting to consider the domains a relic of an older precursor layer preceding the goethite, this might not be the case. The fact that the inner layer composed of goethite was convex towards the steel indicates that the goethite was developing directly at the expense of the latter. Also the fact that, in S2 the veinlets of maghemite and/or magnetite (supposedly based on comparison of similar domains in this sample analyzed by Raman) occur along a tiny internal fractures (Fig. 5) suggests that these developed along this fracture at expense of the original phase, i.e. goethite, or another phase not present anymore. Therefore, the iron oxides are considered an in situ replacement of originally iron hydroxides.

It is interesting to note that the direction of recrystallization, i.e. the oldest phase (goethite) constituting the inner layer of corrosion products around the steel and the secondary iron oxides, notably maghemite, composing the outer layer in our samples differs from the one observed by Demoulin et al. [27] in 46 years old CEM II/A–S concrete. Their type 2a texture involves development of goethite outside a wüstite / magnetite / hematite directly on the steel, interpreted as the mill scale; their type 2b involves development of goethite between this scale and the steel. This mill scale is, however, different from our outer layer of corrosion products, and corresponds texturally to 'our' mill scale (whose composition was not analyzed in this study).

The hematite in our samples might have developed from dehydration and recrystallization of goethite, with magnetite developing due to lack of oxygen supply [38]. This fact might explain why traces of hematite and magnetite are found in the corrosion product layer (i.e. S3). In high Cl^- content environment, the most likely corrosion product phase that forms from ferrihydrate is lepidocrocite, since chlorides stabilize its crystal structure [38]. Though lepidocrocite was not observed in the spot analysis by Raman spectroscopy, it was identified by bulk XRD in S2, S3 and S4. The presence of maghemite marblings (and layers) might be caused by dehydration and recrystallization of lepidocrocite that did not transform into goethite.

Domains with euhedral crystals (S4) - It was clear that corrosion products in air voids outside the mill scale represent iron compounds that had been dissolved prior to deposition. However, also the elongated euhedral crystals with interstitial pores delimined by faces of these crystals observed in the outer layer of corrosion products in S4 (Fig. 8) require free space not available when in situ transformation of steel to goethite to iron oxide occurs. These are considered as having grown from saturated solution in free (partly) fluid filled spaces. Taking the Raman spectrum of spot 3 for S4 (Fig. 16) as a reference, these crystals represent maghemite, indicating that indeed this is at least in part formed by recrystallization.

4.2. Micro-mechanical and -structural characterization of corrosion products

4.2.1. Micro-mechanical properties of corrosion products

In Fig. 18 the range of E_{cp} measured for each specimen was reported.

According to Fig. 18, the average value of E_{cp} formed in different concrete mixtures does not significantly change with cement type, overall ranging between 80−100 GPa in all specimens. This range of E_{cp} is similar to what was found by Hosemann et al. [13] (70−100 GPa) and slightly different from the Elastic modulus of corrosion product studied through nano-indentation by others [7,8,14,15]. Šavija et al. [8] found that E_{cp} ranged between 50−68 GPa, while Zhao et al. [7] measured E_{cp} of two distinct corrosion product layers. In this latter case, they found that the inner layer (formed due to dissolution of the reinforcement) had E_{cp} of 47−86 GPa, while the outer layer (mill scale-related) had 98−122 GPa. Differences with previous studies might be related to the different exposure to which the samples were subjected. Both of these studies investigated the E_{cp} of anodically-polarised (accelerated) corrosion product. Anodic acceleration probably influences the formation and further distribution of corrosion product [8]. The current density at which corrosion was accelerated might influence the micro-structure of the corrosion product, such as its porosity and crystallinity, which likely influence the resulting micro-mechanical properties. Further specimens nano-indented by Zhao et al. [7] included portions of corrosion product previously peeled from a corroding bar, thus excluding the potential effect that the SCI might have on the corrosion product's microstructure (due to constrain from the surrounding concrete). The influence of

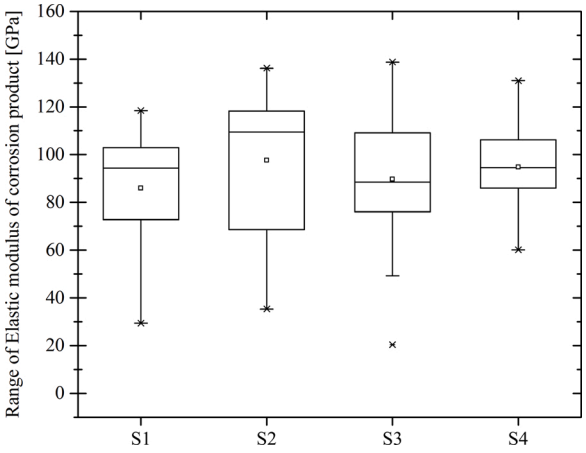

Fig. 18. Range of E_{cp} per specimen, represented by each box. The top, middle and bottom line of the boxes correspond to the 75-, 50- and 25-percentile value (x75, x50 and x25) respectively. The whiskers show the minimum and maximum values, while crosses represent outliners.

boundary conditions (i.e. presence of cracks and cement paste) were already pointed out by Šavija et al. [8], who observed that the elastic modulus of cracked corrosion product was lower than the E_{cp} of undisturbed products. This was because presence of defects and lack of surrounding boundaries that would offer accommodating area for the deformation of the material while being indented, as it was also observed in the present study.

The locations at which cracks occurred varied among the analysed specimens. For S1 and S4, a 5−10 μm wide crack at the interfacial zone between corrosion products and surrounding paste was visible (Figs. 13 and 16). The surroundings of these locations had E_{cp} ranging between 0 and 75 GPa in both cases. Differently, S3 was cracked in proximity to the steel reinforcement (Fig. 15). This crack occurred within the goethite layer, which had E_{cp} ranging between 25 and 75 GPa. For S2, two main locations at the SCI were cracked: the interface between corrosion products and surrounding paste as well as an inner portion coincident to a goethite-maghemite layer. Both these locations had E_{cp} ranging between 0 and 75 GPa. As a matter of fact, it seems that cracks occur at the least resistant locations of the interfacial zone, which however vary among specimens. Three out of four specimens (i.e. S1, S2 and S4) had cracks coincident to the cement paste at the corrosion products-matrix interface. These locations are also adjacent to the mill scale layer surrounding the reinforcement, and they had least E_{cp} according to nano-indentation results. For S1 and S4 an interfacial void (completely and partially) filled by corrosion products is visible, which might have weakened the locations at which cracks are found. On the other hand, S3 had a crack coincident to a goethite layer adjacent to the steel reinforcement (Fig. 15). Interestingly, SEM/EDS analysis suggests that the paste surrounding the reinforcement of this specimens is densely penetrated by corrosion products (Fig. 11). Surrounding paste with penetrated corrosion products is visible also for S2, which however seems less deep and marked than that of S3 according to ESEM/EDS analysis (Fig. 14). Penetration of corrosion products into the surrounding paste probably densified and therefore strengthened the corrosion products-paste interfacial zone, which in this case had E_{cp} ranging between 75 and 100 GPa. On the other hand, the cracked goethite portion of S3 had E_{cp} ranging between 0 and 75 GPa. According to these observations, it seems that penetration of corrosion products into the surrounding paste as well as the presence of interfacial defects can strengthen and weaken the SCI, therefore influencing the locations at which cracks occur.

According to the nano-indentation results of this study (Figs. 9–12), the elastic modulus of pristine steel was higher than its well-known value of 207 GPa. Similar results were obtained by Savija et al. [8], who measured an elastic modulus of pristine steel equal to about 250 GPa. Lower values were obtained by Zhao et al. [7], who obtained an elastic modulus of pristine steel of around 183 GPa. Since in the present study the nano-indenter was calibrated with an external quartz standard prior to each test, the reliability of the results of E_{cp} should not be questioned. At the same time, the difference between the standard elastic modulus of steel and that measured in the present study as well as in previous ones is significant. A possible explanation of these results might be related to the alloy component that is microscopically indented. The microstructure of low-carbon steel is composed of pearlite, a two-phase laminar matrix made of ferrite (α-Fe) and cementite (Fe_3C) [39]. While α-Fe is relatively soft at temperatures below 727 °C, Fe_3C can have an elastic modulus even higher than 300 GPa [40]. The elastic modulus of Fe_3C is recognized to be highly anisotropic, and it depends on, among other parameters, its orientation along different crystallographic directions [40]. A specific orientation of the pearlite structure, and especially of its Fe_3C fraction, might have therefore resulted from the nano-indentation tests in elastic modulus of pristine steel higher than the standard values.

4.2.2. *Relationship between mineralogy and micro-mechanical properties of corrosion products*

The characterization of corrosion products coupling nano-indentation and Raman spectroscopy has been previously conducted by only a few researchers [14,15]. Dehoux et al. [14] characterized the corrosion product compounds and their mechanical properties formed due to different types of corrosion (i.e. artificial corrosion, under controlled chloride environment and naturally generated in ancient buildings). They found that E_{cp} of specific compounds (i.e. goethite, maghemite, magnetite and ferrihydrate) was not varying between samples subjected to different types and time of corrosion. Jiang et al. [15] also found very similar E_{cp} within the samples they analysed in their study, which were corroded through anodic polarization. However, the E_{cp} that they obtained was significantly lower than that of Dehoux et al. [14]. In Fig. 19, the results of E_{cp} for different corrosion product compounds reported by previous studies [14,15] as well as by the present study are reported.

In Fig. 19, it can be seen that similar phases investigated in different studies present different E_{cp}. Compared to previous studies, in the present research higher variation of E_{cp} for specific compounds is visible. This is especially clear for goethite, of which E_{cp} was equal to 92−95 GPa in [14], 67.9 ± 5.3 in [15] and it was varying between 75−125 GPa in the present study. Similar differences can be observed comparing E_{cp} of maghemite and magnetite, for which Dehoux et al. [14] found 113 GPa and 139 GPa, respectively, while Jiang et al. [15] found 82.3 ± 3.7 GPa and103.2 ± 2.7 GPa, respectively. Despite the higher scatter, E_{cp} of maghemite found in S1, S3 and S4 is overall comparable to that found by others. For S2, E_{cp} of both maghemite and magnetite are much lower than that found by others due to the presence of cracks, of which influence on the results has been previously discussed. Furthermore, it is worth mentioning that through nano-indentation the measured E_{cp} was representative for a cluster that is visible only at the sample surface [41]. The main assumption using this technique was that the surface material corresponds to the one indented in depth, which might not be always the case. The specimens analysed in our study were also analysed through X-ray Computed Tomography (CT-scans), as described elsewhere [22]. Through CT-scan analysis, it was verified that corrosion product was present also below the indented locations. However, the fact that superficial characteristics correspond to the in-depth ones could not be verified. Hence, it must be emphasized that the E_{cp} measured in our study as well as that of previous ones were not representative of single corrosion product compounds crystals, but more of clusters formed by precipitation of corrosion products. The micro-mechanical properties of these clusters are likely to be influenced by many inter-related parameters besides their mineralogy, such as their porosity, their crystal orientation and their crystallinity, which differ among different specimens and structures. Therefore, a fixed E_{cp} for specific corrosion product compounds might not be representative for different cases.

Dehoux et al. [14] concluded that corrosion products may evolve over time, due to the consequent transformation of the phases depending on, for instance, the availability of oxygen at the SCI as well as the amount of chlorides in the surroundings. In their study, they observed that the older the specimens were (up to 660 years of age), higher the E_{cp} of the formed corrosion products was. In their opinion, this could be explained by the transformation of the initial phases found in the corrosion product marblings (i.e. ferrihydrate) into more resistant phases (i.e. maghemite and magnetite) during time. In their anodically corroded specimens, Jiang et al. [15] found similar corrosion product mineralogy, but significantly lower E_{cp}. The differences between the results of the two studies were explained by the different environments in which the corrosion products were generated as well as their possibly different crystallinity, crystal size and morphology [15]. In our study, corrosion products with the same mineralogy and age were in some cases found to have different E_{cp} (also from that of previous studies). By looking at the morphology and the E_{cp} of corrosion products, a possible relevant parameter that may influence the micro-mechanical properties of corrosion products at the SCI (and therefore their behaviour) is the porosity of corrosion products. Different morphology and porosity of corrosion products are clearly shown in Fig. 8, in which

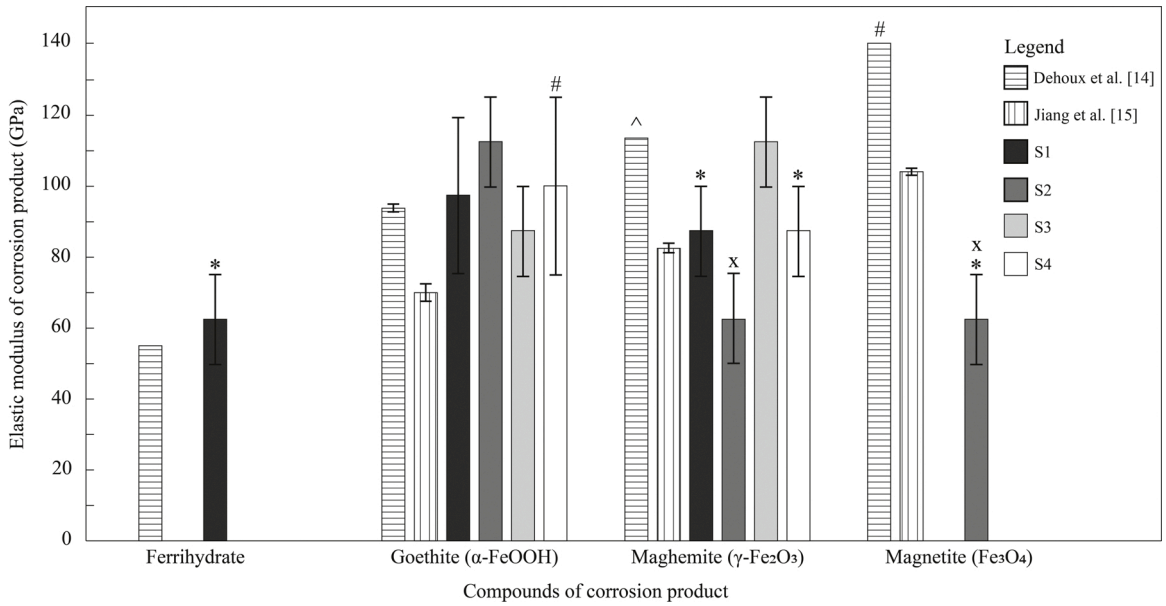

Fig. 19. Comparison of E_{cp} [GPa] of different corrosion product compounds from previous and present studies [14,15]. The whiskers show the minimum and maximum values for each bar. (*=mixed with goethite; #=mixed with maghemite; ^=mixed with ferrihydrate; x = cracked).

randomly-oriented needles of corrosion products with empty spaces as well as overlapping layers that are not completely adjacent to each other are reported. Also, according to the analysis of Fig. 14, corrosion products densely penetrating into the surrounding matrix seem to influence the location at which cracks might occur, strengthening or weakening the interfacial zone. The influence of corrosion products porosity on their E_{cp} would be in line with the results of Dehoux et al. [14], since older specimens (i.e. those that corroded for the longest time) have more corrosion products formed, which would densely accumulate at the interface with a consequent decrease in porosity. Also, anodic acceleration of corrosion would results in more rapid formation of products that are likely less densified than those occurring during decades, which would explain why Jiang et al. [15] found lower E_{cp} for their corrosion products despite they had identical mineralogy of that reported by Dehoux et al. [14]. Coupling these analysis with the transformation of phases depending on the surrounding conditions to which the phases are exposed, it seems that characteristic values for different phases could be only assessed if specifically related to a phase at a specific point in time. These values are likely to change over time due many inter-related parameters, and due to this broad inter-dependency a prediction of their behaviour cannot be accurately established yet.

5. Conclusions

The aim of the present study was to characterize the micro-structure and micro-mechanical properties (i.e. Elastic modulus) of naturally-generated corrosion products due to penetrated chloride ions in reinforced concrete specimens cast with four different cement types: Ordinary Portland (CEM I), Portland-fly ash (CEM II/B), blast furnace slag (CEM III/B) and ternary Portland-fly ash-slag cements (CEM V/A). For this purpose, textures of the corrosion products have been analysed and nano-indentation, NanoSEM-EDS analysis, Raman spectroscopy and X-ray diffraction were conducted. Based on the results of this study, the following conclusions can be drawn:

- -The main corrosion product phases identified were a goethite matrix with marblings and layers of maghemite. Traces of ferrihydrate, magnetite and hematite were also observed, all by Raman spectroscopy. Lepidocrocite was only observed through XRD in three out of four specimens.
- -Corrosion products were mainly developed in situ, but there was evidence that some clusters were formed by precipitation from the pore solution.
- -Goethite was the dominant and oldest corrosion product observed, except possibly for some traces of ferrihydrite. It was partly transformed into hematite and magnetite.
- -Maghemite was also secondary, and at least partially precipitated from the pore solution. The precursor to maghemite was not clear.
- -No significant effect was observed with respect to the effect of cement type on the corrosion product mineralogy and elastic moduli.
- -The E_{cp} of identified corrosion product phases varied within specimens. Furthermore, the E_{cp} obtained in this study slightly differed from those reported by previous researchers [14,15]. It is likely that micro-mechanical properties of phases depend on many inter-related parameters intrinsic to the corrosion product (i.e. porosity, crystallinity, etc.) which could not be assessed. Since these parameters are likely sensitive to changes over time, characteristic values of phases should not be considered as constants.
- -EDS mapping suggest that E_{cp} was inversely proportional to the presence of cracks and the concentration of cement-related components (i.e. Ca and Si), as already pointed out by Savija et al. [8]. Most of the cracks were visible at the interface between the corrosion products and the surrounding matrix and they were coincident to the mill scale layer. When cracks occurred within the corrosion products (i.e. S3) they were found in layers of goethite, which was overall the least resistant compound found in our samples.
- -According to previous studies as well as from the nano-indentation tests and Raman spectroscopy analyses on naturally-generated (chloride induced) corrosion product performed in this study, an average E_{cp} ranging between 80−100 GPa is suggested for use in numerical models for corrosion induced cover cracking related to chloride induced corrosion. In terms of average values, significant variations were not observed between E_{cp} of corrosion product generated in mixes cast with different cement types. These average values would not take into account the different phases and polymorphs that constitute the corrosion product layers.

Funding

This research did not receive any specific grant from funding

agencies in the public, commercial, or not-for-profit sectors.

Author's statement

Emanuele Rossi: Conceptualization, Methodology, Investigation, Writing – Original Draft. **Hongzhi Zhang:** Resources, Writing – Review & Editing. **Santiago J. Garcia:** Resources, Writing – Review & Editing. **Johan Bijleveld:** Investigation, Resources. **Timo G. Nijland:** Investigation, Writing – Review & Editing, Resources, Project administration, Supervision. **Oğuzhan Çopuroğlu:** Investigation, Writing – Review & Editing, Resources, Supervision. **Rob B. Polder:** Investigation, Writing – Review & Editing, Supervision. **Branko Šavija:** Investigation, Writing – Review & Editing, Supervision.

Data availability

The raw/processed data required to reproduce these findings cannot be shared online at this time due to technical limitations, but they are available upon contacting the corresponding author.

Declaration of Competing Interest

The authors report no declarations of interest.

Acknowledgements

The authors would like to thank Mr. Arjan Thijssen of TUDelft and Mr. Willem Duvalois of TNO for their assistance with SEM and XRD analysis.

References

[1] L. Bertolini, B. Elsener, P. Pedeferri, E. Redaelli, R.B. Polder, Corrosion of Steel in Concrete: Prevention, Diagnosis, Repair, JohnWiley & Sons, 2013.
[2] Z. Bazant, Physical model for steel corrosion in concrete sea structures—theory, J. Struct. Div. ASCE 105 (6) (1979) 1137–1153.
[3] J. Molina, C. Alonso, C. Andrade, Cover cracking as a function of rebar corrosion: part 2—numerical model, Mater. Struct. 26 (1993) 532–548.
[4] Y. Liu, R.E. Weyers, Modeling the time-to-corrosion cracking in chloride contaminated reinforced concrete structures, ACI Mater. J. 95 (6) (1998) 675–680.
[5] J. Ozbolt, F. Orsanic, G. Balabanic, M. Kuster, Modeling damage in concrete caused by corrosion of reinforcement: coupled 3D FE model, Int. J. Fract. Mech. 178 (1–2) (2013) 233–244.
[6] B. Savija, M. Lukovic, J. Pacheco, E. Schlangen, Cracking of the concrete cover due to reinforcement corrosion: a two-dimensional lattice model study, Constr. Build. Mater. 44 (2013) 626–638.
[7] Y. Zhao, H. Dai, W. Jin, A study of the elastic moduli of corrosion products using nanoindentation techniques, Corros. Sci. 65 (2012) 163–168.
[8] B. Savija, M. Lukovic, S.A.S. Hosseini, J. Pacheco, E. Schlangen, Corrosion induced cover cracking studied by X-ray computed tomography, nanoindentation and energy dispersive X-ray spectrometry (EDS), Mater. Struct. 48 (2015) 2043–2062.
[9] G.V. Samsonov, The Oxide Handbook, IFI/Plenum, 1973.
[10] A. Ouglova, Y. Berthaud, M. Francois, F. Foct, Mechanical properties of an iron oxide formed by corrosion in reinforced concrete structures, Corros. Sci. 12 (2006) 3988–4000.
[11] K. Bhargava, A.K. Ghosh, Y. Mori, S. Ramanujam, Analytical model for time to cover cracking in RC structures due to rebar corrosion, Nucl. Eng. Des. 11 (2006) 1123–1139.
[12] Y.X. Zhao, H. Dai, H.Y. Ren, W.L. Lin, Experimental study of the modulus of steel corrosion in a concrete port, Corros. Sci. (2011) 17–25.
[13] P. Hosemann, J.G. Swadener, J. Welch, N. Li, Nano-indentation measurement of oxide layers formed in LBE on F/M steels, J. Nucl. Mater. (2008) 201–205.
[14] A. Dehoux, F. Bouchelaghem, Y. Berthaud, Micromechanical and microstructural investigation of steel corrosion layers of variable age developed under impressed current method, atmospheric or saline conditions, Corros. Sci. 97 (2015) 49–61.
[15] B. Jiang, K. Doi, K. Tsuchiya, Y. Kawano, A. Kori, K. Ikushima, Micromechanical properties of steel corrosion products in concrete studied by nano-indentation technique, Corros. Sci. 163 (2020), 108304.
[16] K. Lundgren, Bond between ribbed bars and concrete. Part 2: the effect of corrosion, Mag. Concr. Res. 7 (2005) 383–395.
[17] K. Suda, S. Misra, K. Motohashi, Corrosion products of reinforcing bars embedded in concrete, Corros. Sci. 5-8 (1993) 1543–1549.
[18] S. Caré, Q.T. Nguyen, V. L'Hostis, Y. Berthaud, Mechanical properties of the rust layer induced by impressed current method in reinforced mortar, Cem. Concr. Res. (2008) 1079–1091.
[19] I. Balafas, C.J. Burgoyne, Modelling the structural effects of rust in concrete cover, J. Eng. Mech. 137 (3) (2013) 175–185.
[20] F.J. Molina, C. Alonso, C. Andrade, Cover cracking as a function of rebar corrosion. Part 2: Numerical-model, Mater. Struct. 163 (1993) 532–548.
[21] R.B. Polder, P. Russo, Concrete Resistivity, Corrosion Potential and Corrosion Rate at Young Age As a Function of Cement Type. 98-BT-R1664, TNO Building and Construction Research, Rijswijk, TNO, 1998.
[22] E. Rossi, R. Polder, O. Copuroglu, Nijland, B. Šavija, The influence of defects at the steel/concrete interface for chloride-induced pitting corrosion of naturally-deteriorated 20-years-old specimens studied through X-ray computed tomography, Constr. Build. Mater. 235 (2020), 117474.
[23] W.C. Oliver, G.M. Pharr, Measurement of hardness and elastic modulus by instrumented indentation: advances in understanding and refinements to methodology, J. Mater. Res. 19 (1) (2004) 3–20.
[24] J. Pacheco, O. Çopuroğlu, Quantitative energy-dispersive X-ray microanalysis of chlorine in cement paste, J. Mater. Civ. Eng. 28 (1) (2016), 04015065.
[25] U. Schwertmann, R.M. Cornell, Iron Oxides in the Laboratory, Wiley-VCH, Weinheim, 2000.
[26] R.M. Cornell, U. Schwertmann, The Iron Oxides, VHC Verlagsgesellschaft, Weinhaim, Germany, 1996.
[27] A. Demoulin, C. Trigance, D. Neff, E. Foy, P. Dillmann, V. L'Hostis, The evolution of the corrosion of iron in hydraulic binders analysed from 46-and 260-year-old buildings, Corros. Sci. 52 (10) (2010) 3168–3179.
[28] D.C. Cook, Spectroscopic identification of protective and non-protective corrosion coatings on steel structures in marine environments, Corros. Sci. 47 (10) (2005) 2550–2570.
[29] W.J. Chitty, P. Dillmann, V. L'Hostis, C. Lombard, Long-term corrosion resistance of metallic reinforcements in concrete—a study of corrosion mechanisms based on archaeological artefacts, Corros. Sci. 47 (6) (2005) 1555–1581.
[30] W.J. Chitty, P. Berger, P. Dillmann, V. L'Hostis, Long-term corrosion of rebars embedded in aerial and hydraulic binders–Mechanisms and crucial physico-chemical parameters, Corros. Sci. 50 (8) (2008) 2117–2123.
[31] D. Neff, L. Bellot-Gurlet, P. Dillmann, S. Reguer, L. Legrand, Raman imaging of ancient rust scales on archaeological iron artefacts for long-term atmospheric corrosion mechanisms study, J. Raman Spectros. 37 (10) (2006) 1228–1237.
[32] G.S. Duffó, W. Morris, I. Raspini, C. Saragovi, A study of steel rebars embedded in concrete during 65 years, Corros. Sci. 46 (9) (2004) 2143–2157.
[33] G.S. Duffó, M. Reinoso, C.P. Ramos, S.B. Farina, Characterization of steel rebars embedded in a 70-year old concrete structure, Cem. Concr. Res. 42 (1) (2012) 111–117.
[34] J. Monnier, D. Neff, S. Reguer, P. Dillmann, L. Bellot-Gurlet, E. Leroy, et al., A corrosion study of the ferrous medieval reinforcement of the Amiens cathedral. Phase characterisation and localisation by various microprobes techniques, Corros. Sci. 52 (3) (2010) 695–710.
[35] M. Criado, S. Martínez-Ramirez, J.M. Bastidas, A Raman spectroscopy study of steel corrosion products in activated fly ash mortar containing chlorides, Constr. Build. Mater. 96 (2015) 383–390.
[36] A. Köliö, M. Honkanen, J. Lahdensivu, M. Vippola, M. Pentti, Corrosion products of carbonation induced corrosion in existing reinforced concrete facades, Cem. Concr. Res. 78 (2015) 200–207.
[37] T. Kamimura, S. Nasu, T. Segi, T. Tazaki, H. Miyuki, S. Morimoto, T. Kudo, Influence of cations and anions on the formation of β-FeOOH, Corros. Sci. 47 (10) (2005) 2531–2542.
[38] Y. Song, G. Jiang, Y. Chen, P. Zhao, Y. Tian, Effects of chloride ions on corrosion of ductile iron and carbon steel in soil environments, Sci. Rep. 7 (1) (2017) 1–13.
[39] W.D. Callister, D.G. Rethwisch, Materials Science and Engineering: an Introduction, Wiley, New York, 2018.
[40] G. Ghosh, A first-principles study of cementite (Fe3C) and its alloyed counterparts: elastic constants, elastic anisotropies, and isotropic elastic moduli, AIP Adv. 5 (8) (2015), 087102.
[41] M. Luković, E. Schlangen, G. Ye, Combined experimental and numerical study of fracture behaviour of cement paste at the microlevel, Cement Concr. Res. 73 (2015) 123–135.